

# Directional Metastable Wetting Evolution of Droplets on Artificial Patterned Microcavity Surfaces

Wenshuai Xu, Yu Liu, Boya Xiao, Heng Jiang, Meng Chen,\* and Yuren Wang\*

Controllable wetting transition on artificial microtextured surfaces has significant applications in many industrial fields. In this work, the droplet spreading and the directional wetting transition are investigated on the substrate surface with the patterned microcavities. The results show that the macroscopic inward wetting transition from the periphery to the center of the droplet strongly depends on the mesoscopic sequential transition from Cassie to Wenzel state in the microcavities on the substrate surfaces. The semiquantitative relationship between sagging depth of meniscus in the microcavities and the droplet spreading velocity is set up by utilizing scaling-law analysis in terms of mechanical equilibrium of the meniscus. This finding is expected to help to clarify the issues on the mechanism and main affecting factors of the wetting transition on the patterned surface.

of droplet shapes on superhydrophilic micropillar surfaces. Yuan et al.<sup>[20]</sup> then elaborated the competition between molecular friction at microscale and viscous resistance at mesoscale, and established the scaling laws with respect to energy dissipations. On the macroscopic level, the variance of droplet contour on microtextured patterned surfaces reflects the directional energy dissipation due to the pinning effect of microstructures.<sup>[23–28]</sup> For instance, Raj et al.<sup>[29,30]</sup> developed polygonal droplets shapes by the controllable liquid/solid interaction and proposed predictable criteria for morphology control of droplets on different microtextured surfaces.

## 1. Introduction

Droplet wettability is guided and controlled by artificial microtextured surfaces in many technological applications such as self-cleaning,<sup>[1,2]</sup> droplet recognition,<sup>[3]</sup> water harvesting,<sup>[4,5]</sup> anti-ice,<sup>[6–8]</sup> condensation heat transfer,<sup>[9]</sup> oil–water separation,<sup>[10]</sup> microfluidic devices,<sup>[11–14]</sup> inkjet printing,<sup>[15,16]</sup> and bio-microarrays for DNA and protein chips.<sup>[17,18]</sup> Generally speaking, the dynamic wetting evolution of a droplet on microtextured surfaces depends on not only the macroscopic spreading process and topological changes of droplet shapes, but also the mesoscopic changes of the solid/liquid/vapor triphase interfaces and wetting transition in an isolated cavity. The exploration of clarifying the accurate correlation between mesoscopic and macroscopic features in the droplet wetting process remains ongoing.

In recent years, many researchers were devoted to ascertaining the law of underlying variables for the dynamic wetting process of a droplet on the micro-, meso-, and macroscale levels by utilizing mechanical model and scaling analysis.<sup>[19–22]</sup> Kim et al.<sup>[19]</sup> presented power laws of the temporal evolution


of droplet shapes on superhydrophilic micropillar surfaces. Yuan et al.<sup>[20]</sup> then elaborated the competition between molecular friction at microscale and viscous resistance at mesoscale, and established the scaling laws with respect to energy dissipations. On the macroscopic level, the variance of droplet contour on microtextured patterned surfaces reflects the directional energy dissipation due to the pinning effect of microstructures.<sup>[23–28]</sup> For instance, Raj et al.<sup>[29,30]</sup> developed polygonal droplets shapes by the controllable liquid/solid interaction and proposed predictable criteria for morphology control of droplets on different microtextured surfaces.

On the mesoscale level, the stability of the air–liquid interface on microdecorated surfaces is a key issue and getting intensive attention. There is a growing consensus that both air dissolution<sup>[31]</sup> and interfacial pressure<sup>[32–34]</sup> change the sagging depth of the air–liquid interface in the microcavity on immersion. The entrapped air hinders the spreading dynamics and wetting transition inside the isolated microcavity.<sup>[35,36]</sup> Following the omniphobic and superomniphobic microstructures composed of reentrant and doubly reentrant pillars,<sup>[37–39]</sup> Domingues et al.<sup>[40,41]</sup> designed a landmark omniphobic surfaces with doubly reentrant cavities that can significantly improve the stability of the air–liquid interface and achieve robust entrapment of air upon immersion in wetting liquids. Pendyala et al.<sup>[42]</sup> reported the random and directional wetting transitions of evaporating water droplets on microcavity surfaces with functional nanocoatings and concluded that the time-dependent transition of wetting state is attributed to the evaporation-induced flow within the droplet. However, it is not entirely clear whether the above-mentioned criteria are suitable to interpret the directional and metastable wetting phenomena of sessile droplets without evaporation on microcavity surfaces. In particular, the critical relevance between the macroscopic droplets spreading and mesoscale evolution of the air–liquid interface on microcavity surfaces is far from well understood.

In this work, we demonstrate the association mechanism between mesoscopic evolution of air–liquid interfaces inside microcavities and the droplet spreading phenomenon at macroscale level. To achieve this goal, we investigate the dynamic spreading features and wetting transition of highly wettable and nonevaporative droplets on the polydimethylsiloxane (PDMS) substrate with square arrays of rectangular microcavities. By virtue of the interference-fringe analysis technique, the time-dependent evolution of the air–liquid interface in a microcavity

Dr. W. S. Xu, Y. Liu, B. Y. Xiao, Prof. H. Jiang, M. Chen, Y. R. Wang  
Key Laboratory of Microgravity  
Institute of Mechanics  
Chinese Academy of Sciences  
Beijing 100190, China  
E-mail: chenmeng@imech.ac.cn; yurenwang@imech.ac.cn

Dr. W. S. Xu, Y. Liu, B. Y. Xiao, Prof. H. Jiang, M. Chen, Y. R. Wang  
University of Chinese Academy of Sciences  
Beijing 100049, China

 The ORCID identification number(s) for the author(s) of this article can be found under <https://doi.org/10.1002/admi.202100174>.

DOI: 10.1002/admi.202100174

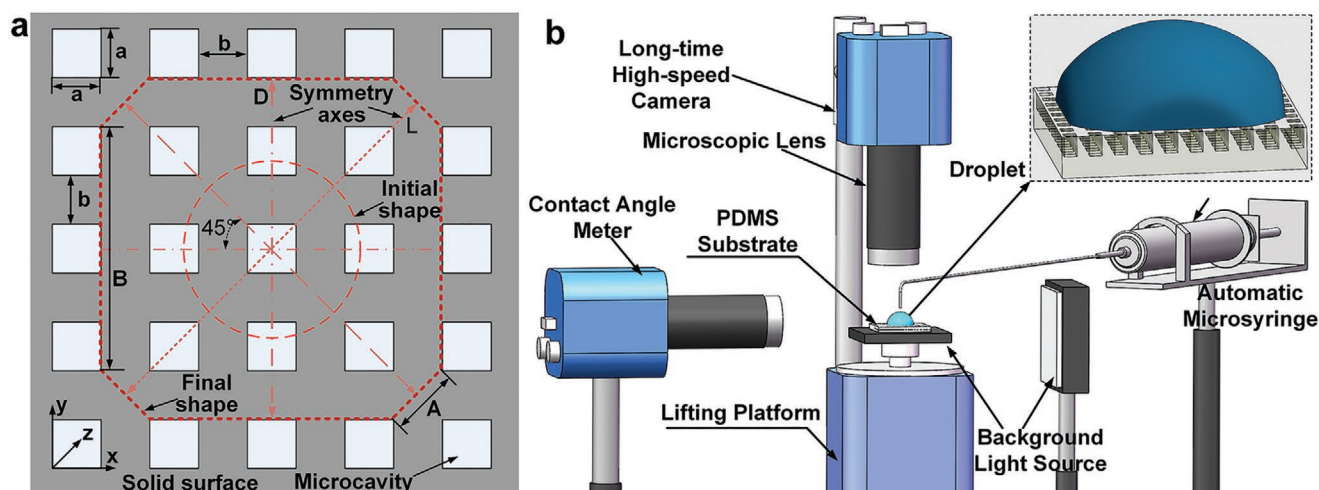


**Figure 1.** Schematics. a) The microcavity pattern design. The predicted droplet shape is marked by the red line.  $D$  and  $L$  are two symmetry axes of the droplet shape;  $A$  and  $B$  are sides of the droplet shape. b) Experimental setup and final droplet shape.

and droplet shapes are monitored simultaneously for a long time. The scaling laws of the macroscopic liquid spreading and mesoscopic interface-wetting transition are obtained under various experimental conditions with controlled variables. The time-dependent mechanism of directional wetting transition was clarified by establishing an evolutionary model of the air-liquid interface on microcavity surfaces.

## 2. Results and Discussion

The patterned microcavity arrays on PDMS substrates were prepared using soft lithography (Figure S1, Supporting Information). The geometrical parameters including length ( $a$ ) and pitch ( $b$ ) are defined in Figure 1a, where  $a = 30 \mu\text{m}$  and pitch  $b$  changes from 18 to  $70 \mu\text{m}$  (Table 1). The depth ( $h$ ) of all cavities is  $50 \mu\text{m}$ . The texture area fraction is defined as  $\Phi_s = a^2 / (a+b)^2$ . The irrelevant factors including evaporation, droplet volume, dropping speed, and gravity were strictly controlled. Hydrophilic nonvolatile silicone oils with different viscosities were used in experiments (Table S1, Supporting Information). For a  $4 \mu\text{L}$  droplet, the initial radius  $R_0$  is  $0.82 \pm 0.03 \text{ mm}$ , which is smaller than the capillary length  $R_{\text{cap}} = \sqrt{\gamma_{\text{LV}} / (\rho g)}$ , where  $\gamma_{\text{LV}}$ ,  $\rho$ , and  $g$  are the air-liquid surface tension, liquid density, and gravitational acceleration, respectively. The initial falling velocity,  $v_0$ , of droplets was negligible (The Weber number ( $We$ ) for all experiment conditions is less than  $4.25 \times 10^{-5}$ , where  $We = 2\rho R_0 v_0^2 / \gamma_{\text{LV}}$ ). Hence, surface tension rather than gravity dominates the wetting process. The experimental setup is shown in Figure 1b, and the experimental conditions are listed in Table 1.

### 2.1. Macroscopic Phenomena of Wetting Transition on Microcavity Surfaces

When the droplet is deposited on microcavity surfaces, dynamic wetting behaviors including liquid movement, contact-line pinning and depinning, and air-liquid interface evolution changes

with liquid spreading. The underlying air packet will be trapped and isolated within the microcavities while an individual cavity is not connected with others. The contact line and air-liquid interface on microcavity surfaces could be clearly observed in experiments from the top-view by interference fringes.<sup>[42,43]</sup> The term “air-liquid interface” in this paper specifically refers to the interface between the air and liquid phases in a microcavity on immersion in liquid. Other researchers have found similar directional wetting transition with sessile water droplet on the hydrophilic microcavity surfaces,<sup>[42]</sup> where the droplet shape is irregular and greatly affected by surface topography due to the

**Table 1.** Morphologic parameters of microcavity-arrayed substrates ( $h = 50 \mu\text{m}$ ).

Number of conditions	Liquid Viscosity $\mu$ [ $\text{mm}^2 \text{s}^{-1}$ ]	Sample	$a$ [ $\mu\text{m}$ ]	$b$ [ $\mu\text{m}$ ]	$\Phi_s$
F1	50	Smooth PDMS	–	–	–
F2	350				
F3	1000				
1	50	S1	30	70	0.09
2	350				
3	1000				
4	50	S2	30	20	0.36
5	350				
6	1000				
7	50	S3	30	44	0.16
8	350				
9	1000				
10	50	S4	30	23	0.32
11	350				
12	1000				
13	50	S5	30	18	0.39
14	350				
15	1000				

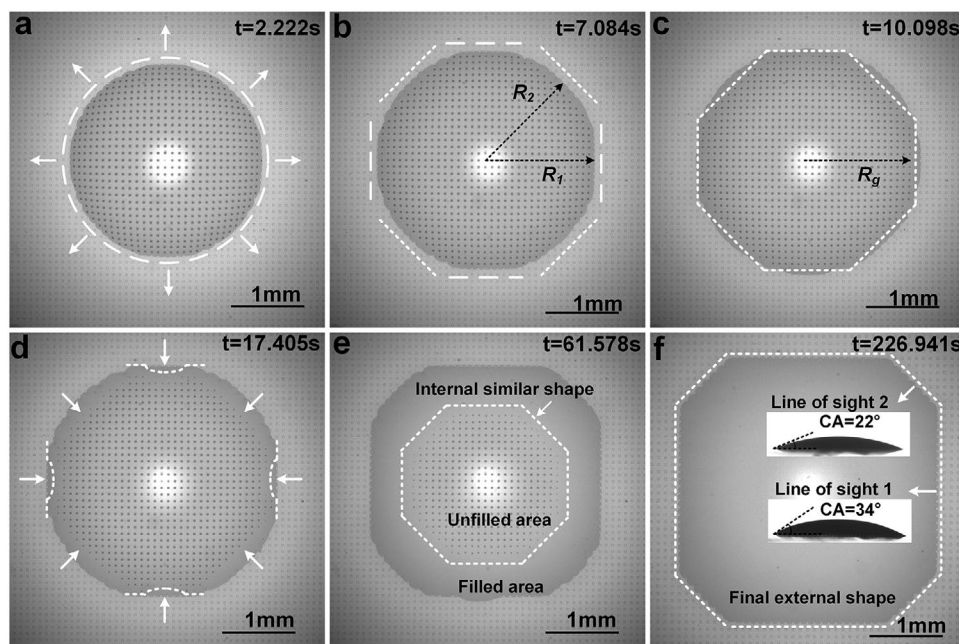


**Figure 2.** The temporal evolution of a spreading droplet on a microcavity surface (Experimental condition 3). a) Circular contour of the initial rapid-spreading stage. b) Droplet shape transformed from circle to octagon. c) Octagonal boundary of the region of metastable air–liquid interfaces. d) Incipient stage of directional wetting transition from the periphery to the center of the droplet. e) Octagonal internal boundary of metastable air–liquid interfaces and the droplet shape. f) Final octagonal droplet shape. The wetting evolution of microcavities is shown using white boundaries and arrows. The black spots inside the droplet indicate the metastable air–liquid interfaces in microcavities.  $R_1$  and  $R_2$  represent the distances from the droplet center to the outermost contact line along lines of sight 1 and 2, respectively.  $R_g$  is defined as the horizontal distance from the droplet center to the outermost microcavity with the air–liquid interface along line of sight 1. The value of  $R_g$  changes with time and is smaller than  $R_1$ . The quantity  $R_{gmax}$  is the maximum value of  $R_g$  during the entire spreading stage.

high surface tension ( $72 \text{ mN m}^{-1}$ ) and low viscosity ( $\approx 1 \text{ mPa s}$  at  $20^\circ \text{C}$ ). In present work, we observed the directional wetting transitions of regular droplet shapes from Cassie to Wenzel state on microcavity surfaces and noted important events by using silicone oils. The dynamic wetting process of droplet spreading and directional wetting transition was divided into four stages (Figure 2)

- (I) The first stage was the rapid-wetting state from the initial deposition to the appearance of obvious pinning phenomena (Figure 2a,b). With the rapid spread of circular droplets, the air in the microcavities was entrapped. Gravitational energy was rapidly released and converted into the kinetic energy and surface energy in the Cassie stages.<sup>[44]</sup> At the same time, the kinetic energy of droplet got transferred to surface energy with the increase of spreading area.<sup>[45]</sup>
- (II) As the kinetic energy of the droplet decreased, the local contact line was pinned at the cavity edges (Figure 2b,c), causing subsequent liquid accumulation at contact line. During this process, the liquid always broke through the pinning effect of microcavity array from the center of both sides A and B. The contact-line speeds were different along lines of sight 1 and 2 due to the unequal microcavity densities. This induced that the droplet contour transformed from a circle to an octagon. Microcavities at the edge of contour along the line of sight 1 gradually filled. Meanwhile, as shown in Figure 2c, the air–liquid interface remained stable within the white-line region.

- (III) Microcavities near the external contact line were gradually filled with liquid. As shown in Figure 2d, the air–liquid interface in the microcavities near the contour area became unstable. The time-dependent wetting transition (Cassie-to-Wenzel) from the periphery to the center of the droplet was obviously observed in Figure 2d,e. During this process, an interesting phenomenon was that the connecting contour line between the isolated outermost unfilled microcavities underneath the sessile droplet was similar to the octagonal droplet shape (Figure 2e; Movies S1–S5, Supporting Information). The temporal evolution reveals the air–liquid interfaces with the largest distance  $R_{gmax}$  disappear first, while the air–liquid interfaces in the droplet center ( $R_g = 0$ ) vanish last. This provides an inspiration that there may be correlations between mesoscopic evolution of air–liquid interfaces inside microcavities and the droplet spreading.
- (IV) Finally, the sessile droplet reached a complete Wenzel state with an octagonal exterior contour (Figure 2f), while all the microcavities were filled with liquid.

In the wetting process, the equilibrium contact angles ( $\theta_{eq}$ ), advancing contact angles ( $\theta_{adv}$ ), and receding contact angles ( $\theta_{rec}$ ) of all experimental conditions were obtained (Figures S2a and S3, Supporting Information). The results showed that the values of  $\theta_{eq}$ ,  $\theta_{adv}$ , and  $\theta_{rec}$  along lines of sight 1 were larger than those along lines of sight 2 (Section S1, Supporting Information). There is a negative correlation between the values of  $\theta_{eq}$  and  $\Phi_s$ . In addition, the maximal wetting area of droplet



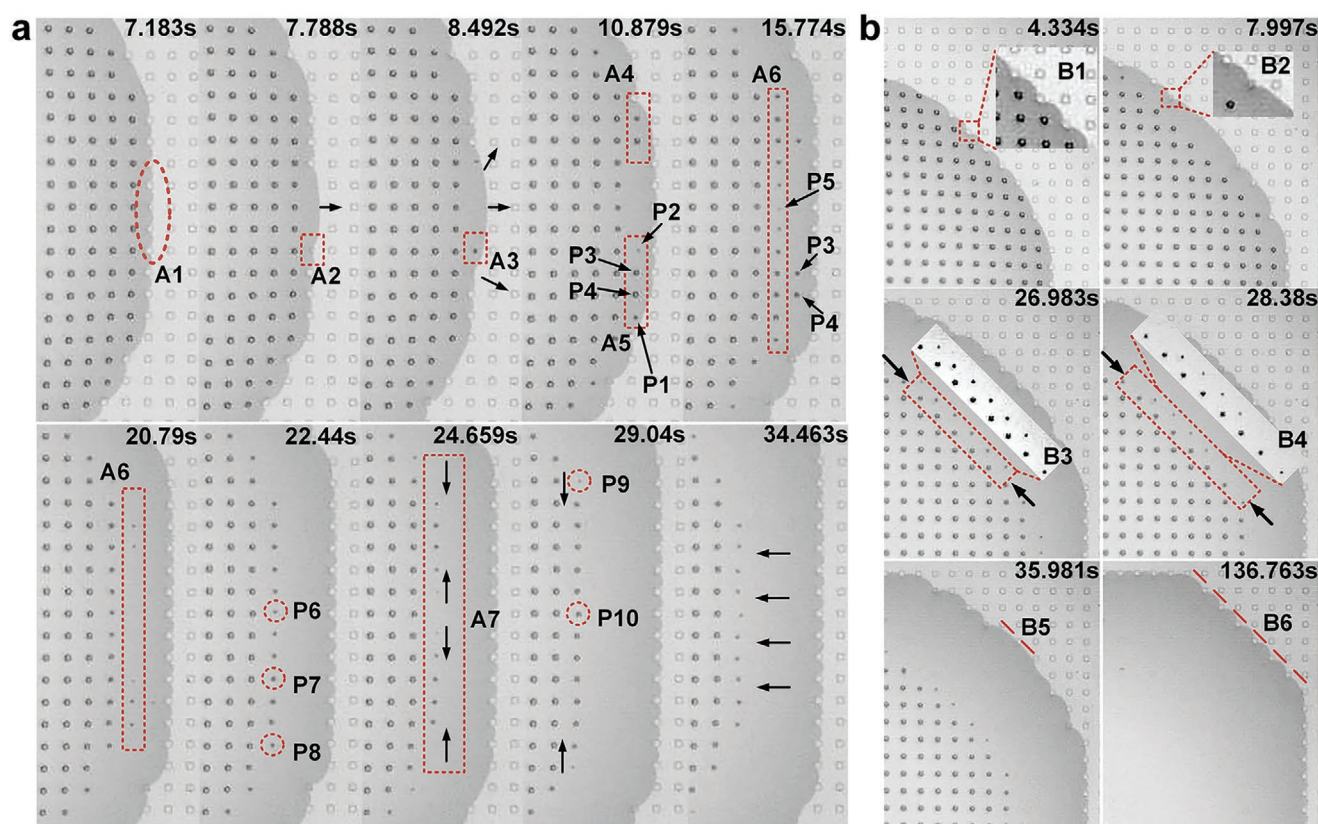


**Figure 3.** Time-dependent sequence of snapshots for experimental condition 3 in the direction of a) sight 1 and b) sight 2. The light black spots are the unfilled cavities.

in a stable Wenzel state was affected by  $\Phi_s$  and liquid viscosity (Figures S2b and S4, Supporting Information).

For the transition of air–liquid interface in microcavities, the sessile droplet showed distinct time sequences and more details along two lines of sight (Figure 3). First, the microcavities in area A1 were filled slowly as the contact line advanced. Then, liquid spread to the perpendicular channel between the two arrays and finally reached a quasi-equilibrium state before the process repeated. One of the details to note is that the curvature of the contact line occurred at the initial contact position of a microcavity due to the edge effect of sharpened corner, which is different from the pinning condition on the micropillar surface.<sup>[46]</sup> The curvature in area A2, made a local Laplace pressure to promote liquid spreading between the two rows of microcavities.<sup>[20]</sup> The liquid film in areas A3–A5 maintained a metastable state with trapped air in the microcavities. After that, the transition of the air–liquid interfaces in the microcavities demonstrated a time-dependent wetting behavior from the Cassie to the Wenzel state. For instance, the air–liquid interfaces at points P1 and P2 disappeared earlier than those at P3 and P4. After a few seconds, the air–liquid interfaces at P5 of area A6 first became unstable and disappeared. From 22.44 to 24.659 s, paths of disappearance of the air–liquid interfaces in the cavities simultaneously occurred from P6 to P7 and P8 to P7 in area A7. However, after the evolution of the outermost arrays, the evolution path moved from the outside (P9) to the inside position (P10) along the line of each

array and exhibited a radially inward transition (Movies S1, Supporting Information).

Meanwhile, the contact line moved forward along the line of sight 2 (Figure 3b). In area B1, the contact line was transiently pinned by the microcavities. Then, the microcavities were gradually filled with liquid in area B2. In the later stage, the kinetic energy at the contact line was too little to break through the pinning effect of a microcavity. At the same time, the silicone oil eventually infiltrated the microcavity from the edge to the center. Finally, all of the microcavities were filled with liquid by repeating the above law, and the contact line in B6 was firmly pinned. The wetting system of sessile droplet eventually reached a stable Wenzel state to keep thermodynamic equilibrium. These phenomena were suitable to all experimental conditions in Table 1 (Movies S1–S5, Supporting Information).

## 2.2. Mechanism of Directional Wetting Transition

When the droplet spreads horizontally and encounters a sharp corner of cavity edge, the local contact angle increases due to the edge effect (Figure 4a). The sharp edges of cavity has an evident pinning effect for the liquid film, resulting in the significant increase of local contact angle from  $\theta_{adv}$  to  $\theta_{max}$  at the contact line.<sup>[47–49]</sup> The maximum local contact angle ( $\theta_{max}$ ) at the cavity edge is greater than  $90^\circ$  (Figure 4b,c). The pinning force reaches a maximum at the depinning moment and is always in the

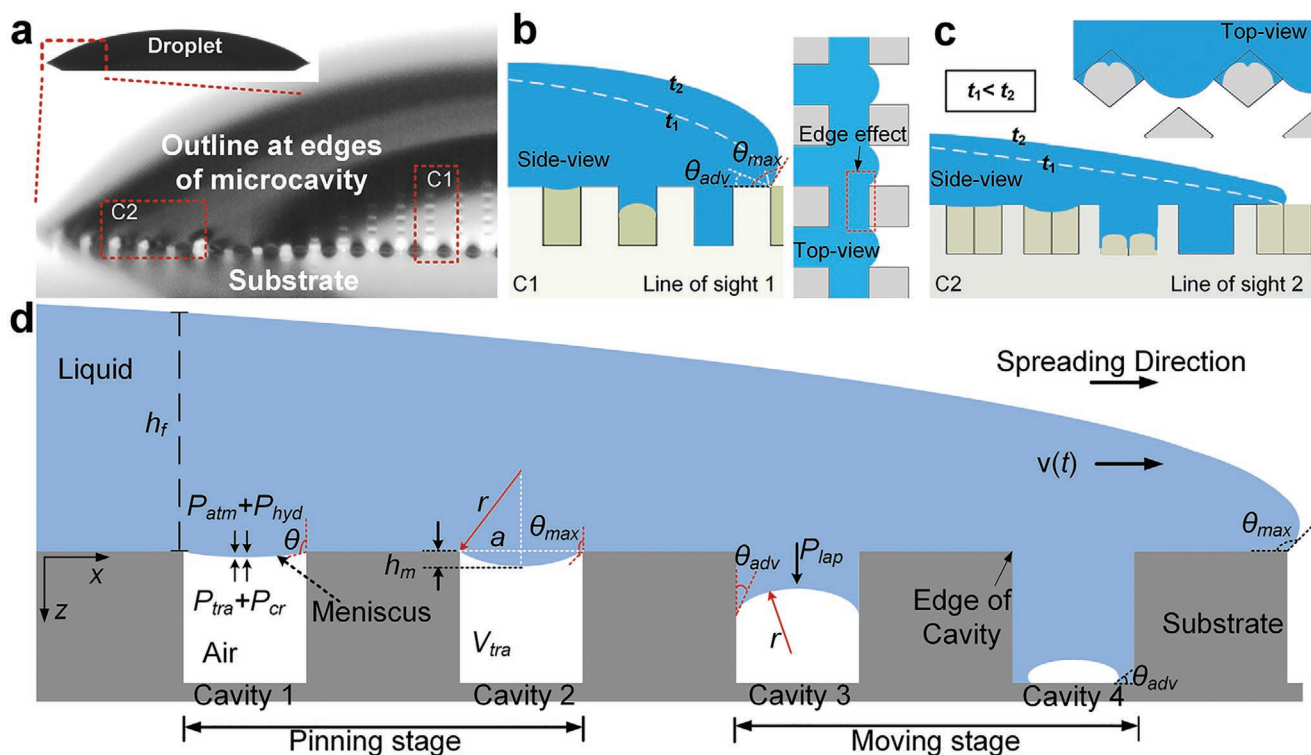


**Figure 4.** a) Side-view of sessile droplet on microcavity surfaces. Schematics of directional wetting transition in b) line of sight 1 and c) the line of sight 2. d) Schematics demonstrating the air–liquid interface evolution and pressure balance in microcavities.

opposite direction of the movement trend of the liquid.<sup>[22,50,51]</sup> When the liquid tends to squeeze into the microcavity, due to the strong edge effect of the small microsize of microcavity, the meniscus of wetting liquid at the entrance of microcavity vertically sagged at the initial pinning stage (Figure 4d).<sup>[41]</sup> Other researchers also found that even hydrophilic surfaces showed hydrophobicity near the edge of microcavity.<sup>[42]</sup> Moreover, the square microcavity can be considered as capillary tube with square cross section,<sup>[52]</sup> where the wetting transition occurs more easily than that in circular microcavities.<sup>[41]</sup> The corners inside square microcavity will promote liquid imbibition,<sup>[53]</sup> causing the lower position of the air–liquid interface at the corners than main meniscus at the center of microcavity (Figure S5, Supporting Information). Thus, the mechanical equilibrium of the air–liquid interface, the hydrophilic contact angle of the wall and imbibition of wetting liquids along the corners determine the shape of the meniscus in the moving stage (Figure 4b–d; Figure S5, Supporting Information).

The air–liquid interface in the microcavities can be simplified as a meniscus from the lateral 2D profile (Figure 4d). The reason for time-dependent wetting transition is that, at the same dissolution rate, the entrapped air in the microcavity dissolves in liquid within different time horizon.<sup>[32,54]</sup> The temporal wetting characteristics reveal that the entrapped air volume ( $V_{tra}$ ) in a microcavity is different. In Figure 4d, the height from the center of the main meniscus to the contact line in the cavity sidewall is defined as  $h_m$ , which is directly related to  $V_{tra}$ . Hence, the initial values of  $h_m(0)$  are different after the liquid depositing over the microcavities. Moreover, if the meniscus is instantly in the moving stage after the liquid depositing on

the surface, the initial position of the main meniscus  $h_m(0)$  needs to compensate for the distance  $h_d$ . Hence,  $h_m(0) = h_d - h_m$ , where  $h_d$  is the distance from the edge of microcavity to the contact line on the sidewall. However, the exact value of  $h_m(0)$  of every microcavity cannot be obtained experimentally for now. It is feasible to do a qualitative analysis of  $h_m$  through other physical parameters. Figure 4d shows that by judging whether the contact line breaks away from the edge of the microcavity, the movement of meniscus is divided into “pinning stage” and “moving stage.” At the end of pinning stage, when the contact line begins depinning, the height  $h_m$  of meniscus reaches maximum that depends on maximum contact angle  $\theta_{max}$  and the size of the cavity.<sup>[42]</sup> Then, the evolution of liquid meniscus turns into an irreversible moving stage. Therefore,  $h_m(0)$  is a key factor in the whole evolution of the air–liquid interface inside a microcavity.

The air–liquid interface evolution can be reduced to a 1D problem along the central longitudinal profile (Figure 4d).<sup>[31]</sup> The pressure balance at the meniscus is assumed to be a quasi-equilibrium obeying the equation

$$P_{cr} + P_{tra} = P_{atm} + P_{hyd} \quad (1)$$

where  $P_{cr} \approx P_{lap} + P_{vap} + P_{flow}$  is a collection of pressures including capillary pressure  $P_{lap}$ , vapor pressure  $P_{vap}$ , evaporation-induced pressure  $P_{flow}$ ;  $P_{tra}$  is the entrapped air pressure in the microcavity;  $P_{atm}$  is atmospheric pressure; and  $P_{hyd} = \rho gh_f$  is the hydrostatic pressure, where  $h_f$  is the height from the liquid surface to the main meniscus. Silicone oil does not evaporate, which means that  $P_{vap} = 0$  and  $P_{flow} = 0$ . The ideal gas law with the isothermal

assumption can be expressed as  $P_{tra}(t) = P_{atm} V_0 / V_{tra}(t)$ , where  $V_0 = a^2 h$  is the volume of a single microcavity. According to the Laplace equation, capillary pressure  $P_{lap}$  can be expressed as  $P_{lap} = -2\gamma_{LV} \cos\theta / r$ , where  $\theta$  is the instant contact angle and  $r$  is the radius of meniscus. In the pinning stage, the liquid meniscus with a smaller curvature radius will provide greater Laplace pressure to resist the wetting transition (e.g., Cavities 1 and 2 in Figure 4d). However, in the moving stage, the Laplace pressure will prevent entrapped air from escaping from the microcavity (e.g., Cavities 3 and 4 in Figure 4d). Assuming that the meniscus is a spherical surface,  $r$  relates to  $\theta$  via  $r = a / 2\cos\theta$ . According to Equation (1), the meniscus radius  $r$  can be obtained by substituting the relevant parameters of air dissolution

$$r = \begin{cases} \sqrt{\frac{\gamma_{LV} a}{p_{atm} (1 - V_0 / V_{tra}(t)) + p_{hyd}}}, & \text{at pinning stage} \\ a / 2\cos\theta_{adv}, & \text{at moving stage} \end{cases} \quad (2)$$

There is a geometric relationship between  $h_m$  and  $r$  via  $h_m = r(1 - \sin\theta)$ . According to Equation (2), the value of  $h_m$  varies as  $V_{tra}$  at the pinning stage and becomes constant at the moving stage. The entrapped air dissolves in the silicone oil, causing the air–liquid interface to move until the microcavity was completely filled. According to Fick's law<sup>[55]</sup> and Henry's law,<sup>[56]</sup> the dissolution rate through the air–liquid interface is proportional to the entrapped air pressure  $P_{tra}$  and meniscus area  $A_m(t)$ , and the dissolution exchange mainly occurs in the air diffusion layer. The air dissolution rate is expressed as<sup>[57]</sup>

$$\frac{dV_{tra}(t)}{dt} = K_c A_m(t) [p_{atm} + p_H - p_{cr} - cK_h] \quad (3)$$

where  $A_m(t)$  is the meniscus area related to radius  $r$ , which only changes in the pinning stage and is a constant at the moving stage;  $K_c$  is the mass transfer coefficient of air at the air–water interface;<sup>[58]</sup>  $K_h$  is Henry's constant;<sup>[56]</sup>  $c$  is the molar fraction solubility of air in silicone oil; and  $cK_h$  represents the partial pressure of dissolved air in silicone oil. If the effect of temperature is ignored,  $c$  can be expressed in terms of the Bunsen solubility  $\delta$  of air in silicone oil as  $c = \delta / (1.375 + \delta)$ , where  $\delta = P_{tra} / P_{atm} \times e^{\alpha + \beta/T}$  can be obtained via solubility experiments, and  $\alpha$  and  $\beta$  are constants obtained by fitting.<sup>[59]</sup>

From the above mechanical analysis, we found that the initial meniscus position  $h_m(0)$  of the air–liquid interface corresponding to the initial entrapped air volume  $V_{tra}(0)$  affected the total wetting transition time  $t_{max}$  of the air–liquid interface in the microcavity. This means  $h_m(0) \sim V_{tra}(0) \sim t_{max}$ . Therefore, the evolution of the air–liquid interface at the mesoscopic scale can be related to the macroscopic spreading behavior by statistically analyzing factors such as wetting transition time.

### 2.3. Scaling Law of Droplet Propagation and Directional Wetting Transition

Macroscopically, the dimensionless radius  $R_x/R_0$  is related to the dimensionless time  $\tau = t\gamma_{LV}/\mu R_0$ , where  $x \in [1, 2, g]$ . In the

early rapid-spreading state, the dimensionless droplet radius and spreading time on a microcavity surface fit well with the power function  $R_x/R_0 \sim \tau^n$  (Figure 5a,b; Figures S6a, S7, S8a,b, S9, and S10, Supporting Information), which is similar to experimental results on a microcolumn surface.<sup>[20]</sup> Considering the propagation of droplets on flat surfaces, the scaling exponent  $n$  satisfies  $2/25 < n < 1/10$  (Figure S6a and Table S2, Supporting Information). Under the assumption of lubrication approximation (Section S2, Supporting Information), the scaling exponent reveals that energy dissipation is dominated by mesoscale viscous resistance when kinematic viscosity is high; when the liquid viscosity decreases, the contribution of the molecular friction becomes more important.<sup>[19]</sup>

The scaling indices are much larger on microcavity surfaces than on smooth surfaces in the first spreading stage (I). In the log–log plots of Figure 5a,b for experimental conditions 1–3, the directional spreading radii  $R_1/R_0$  and  $R_2/R_0$  on substrate S1 obeys scaling index of  $1/10 \leq n \leq 1/5$ . The scaling indices in increasing order correspond to conditions 1, 2, and 3, representing increasing droplet viscosity. This reveals that the energy dissipation rate grows faster as the proportion of viscous resistance increases in the total energy dissipation. However, because of the pinning of microcavity arrays, the power law is inapplicable after the early spreading period, where radius versus time becomes a step curve. The droplet spreads for a long time between the two arrays as energy dissipates and liquid accumulates (step curve stage in Figure 5a,b).

There are two macroscopic transition stages during the evolution of air–liquid interfaces (Figure 5c,d): rapid generation (stage 1) and the directional wetting transition (stage 2). The maximum wetting area and the radius of air–liquid interfaces  $R_{gmax}$  decreased as the microcavity density  $\Phi_s$  increased (Figure 5c; Figure S4, Supporting Information). For the directional wetting transition, the experimental results showed that as the microcavity density increased, the outermost wetting transitions occurred later. In Figure 5c, the values of the maximum evolution time  $\tau_{max}$  in descending order correspond to testing conditions 15, 6, 12, 9, and 3, under which the microcavity density  $\Phi_s$  was 0.39, 0.36, 0.32, 0.16, and 0.09, respectively. The order was the opposite to the maximum outermost air–liquid interface radius  $R_{gmax}$ . Given the influence of droplet viscosity, Figure 5d illustrates that the maximum dimensionless evolution time  $\tau$  increases with decreasing viscosity  $\mu$ . This result indicates that  $\tau_{max} \propto \Phi_s/\mu$  and  $R_{gmax} \propto (1 - \Phi_s)\mu$ , and that the air–liquid interface transition of a microcavity is affected by the properties of the solid–liquid and air–liquid interfaces. According to the fitting curves in Figure 5c,d, the wetting transitions in stage 2 approximately fit the power-law function  $Y = I_1 + I_2 X^n$ . We found that parameter  $I_1$  relates to the maximum value of  $R_{gmax}$ , while values for  $I_2$  and  $n$  are relatively unordered (Table S3, Supporting Information). Therefore, the evolution of air–liquid interfaces follow the relationship  $(R_{gmax} - R_g)/R_0 \sim \tau^n$  (Figures S6b and S8d, Supporting Information). Between stages 1 and 2, the Cassie state clearly underwent change related to the texture area fraction  $\Phi_s$  and liquid viscosity  $\mu$ . For instance, when  $\Phi_s = 0.39$ , the duration of the outermost Cassie state was longer than that in other conditions (Figure 5c).

The slope changes of the experimental curves in Figure 5a,b show that the speed of droplet spreading  $v(t)$  at the initial



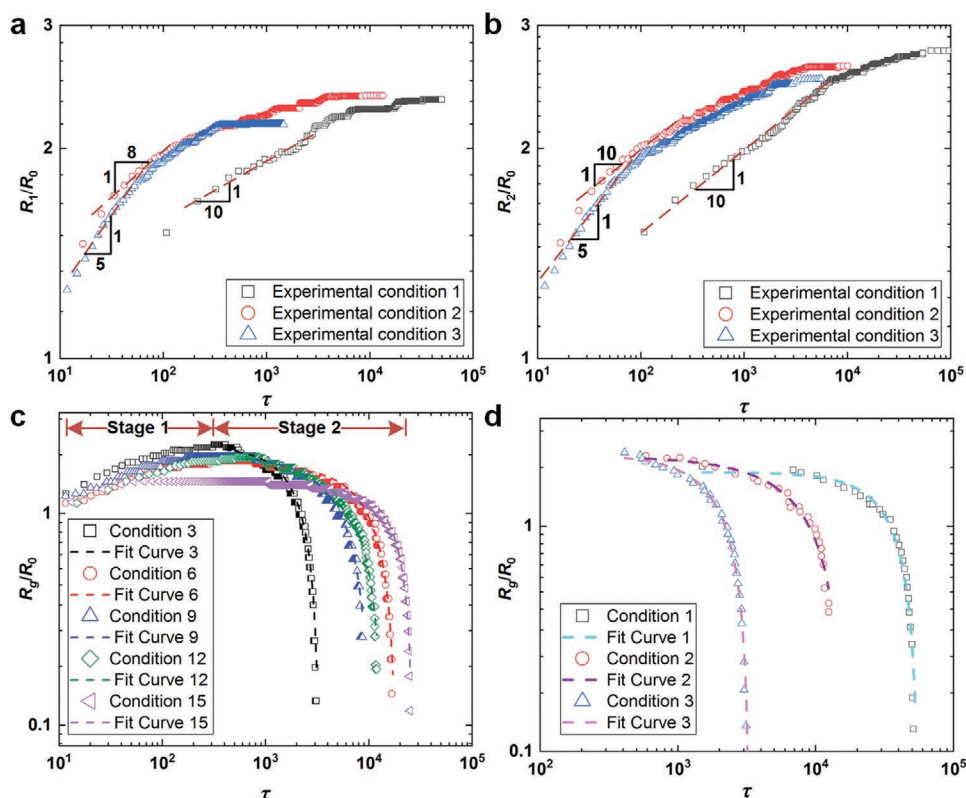


**Figure 5.** Propagation of dimensionless liquid spreading radii a)  $R_1/R_0$  and b)  $R_2/R_0$  with respect to time  $\tau$  under the different experimental conditions listed in Table 1. c) Dimensionless distance  $R_g/R_0$  with respect to time  $\tau$  during the total droplet spreading process under different conditions. The generation (stage 1) and disappearance (stage 2) characteristics of air–liquid interfaces can be expressed in terms of the distance  $R_g/R_0$  and time  $\tau$ . The duration of air–liquid interface evolution at a microcavity is obtained from the different time  $\tau$  with the same value of  $R_g/R_0$  in stages 1 and 2. d) Dimensionless distance  $R_g/R_0$  with respect to time  $\tau$  for droplets with different viscosities on substrate S1. The scatter plots represent experimental data, and the dashed lines are fitted curves using power law functions. The parameters of the fitted lines are listed in Table S3 in the Supporting Information.

stage is faster than that at later stage, which correlates with parameter  $R_x$  via  $R_x \propto \nu(t)^{-1}$ . The wetting transition time  $t_{\max}$  of the air–liquid interface at a specific value of  $R_x$  can be found in Figure 5c, where  $t_{\max} \propto R_x^{-1}$ . From the relationship ( $h_m(0) \sim V_{\text{tra}}(0) \sim t_{\max}$ ) in Section 2.3, the initial bending height  $h_m(0)$  of the air–liquid interface has an indirect negative correlation with the liquid-spreading speed  $\nu(t)$  that can be expressed as  $h_m(0) \propto \nu(t)^{-1}$ . The influence of liquid spreading speed on the shape of the initial meniscus can be considered as a one-off. Hence, by synthesizing the mesoscopic analysis (Figure 4) and macroscopic experimental results (Figure 5), we obtained the semiquantitative relationship  $h_m(0) \propto V_{\text{tra}}(0)^{-1} \propto \nu(t)^{-1} \propto R_x \propto \tau_{\max}^{-1}$ . From the power-law relationship between  $R_x$  and  $\tau^i$ , we can assume that there are power-law relationships between  $h_m(0)$  and  $\nu(t)$ .

### 3. Conclusion

In summary, droplet spreading laws and the evolution of the air–liquid interface in a microcavity were obtained by analyzing wetting behavior on microcavity surfaces. The shape of a sessile droplet on a square microcavity array surface evolved into an octagon due to the variance of energy dissipation in various directions. The relationship between spreading radius and time

in the early spreading stage obeyed the power law  $R_x/R_0 \sim \tau^i$ , while the relationship in the later stage was manifested as a step curve owing to the rapid energy dissipation caused by pinning effect. The macroscopic wetting transition of air–liquid interfaces also fitted the power law  $(R_{g\max} - R_g)/R_0 \sim \tau^i$ , which depended on the microcavity density and liquid properties. The mechanism analysis revealed that the directional wetting transition is ascribed to the initial position of the air–liquid interface with time-dependent spreading velocity. The analysis further uncovers that the basic mechanism of wetting transition is that the dissolution of entrapped air in a microcavity leads to the change of mechanical equilibrium on the air–liquid interface. This work is expected to provide a new explanation to help clarify the issues on the mechanism and main affecting factors of the wetting transition on the patterned surface. It also may give us a guide for deep understanding of engineering problems on microdecorated surfaces such as the probable inhomogeneity of nanoparticles self-assembly, droplet viscosity measurement, and liquid wetting control.

### 4. Experimental Section

**Preparation of PDMS Substrates:** Artificially designed rectangular microcavity arrays on the PDMS substrates were prepared by soft lithography technology. First, the photoresist layer (SU8-25,  $50 \pm 5 \mu\text{m}$

thick) was spin-coated on a clean 6-inch hydrophilic silicon wafer. Subsequently, a lithography mask (manufactured by New Way Photomask Making Co., Ltd. Shenzhen, China) was used to cover the photoresist layer. Afterward, the desired pattern was generated in a photoresist layer after photolithography. Then, a chemical vapor phase procedure (1H, 1H, 2H, 2H-perfluorodecyltrioxydimethylsilane, Aladdin) was applied to form the hydrophobic molecular layer in the surface layer. After sufficiently mixing and degassing purification, the PDMS (Sylgard 184, Dow Corning, USA) was poured onto the mold and placed in a vacuum oven at 80 °C for 2 h. After refrigeration, the PDMS layer (thickness ≈ 2 mm) with microcavity pattern structures were carefully separated from the photoresist mold. The size residual of actual fabricated microstructure sample was within an acceptable range (<2%). Before every test, the substrates were cleaned and washed with isopropyl alcohol, ethanol (Sinopharm Chemical Reagent Co., Ltd. China), and deionized water (ultrasound for 10 min). Then, the PDMS substrates were placed on a clean glass sheet and dried with high-purity nitrogen.

**Contact Angle Measurement:** Dimethicone (XIAMETER PMX-200 silicone fluid) were used as the test droplet and purchased from Dow Corning Co., Ltd., USA (Table S1, Supporting Information). The apparent contact angles of the droplets on the samples were measured using the automatic contact angle measuring instrument (OCA15EC, DataPhysics Instruments GmbH, Germany). Droplets within  $4 \pm 0.5 \mu\text{L}$  were advanced/receded at a rate of  $0.1 \mu\text{L s}^{-1}$  by precise liquid injection. To eliminate the influence of falling gravitational potential energy, the droplets could exactly touch the substrates when separated from syringe needle. All the data were analyzed by SCA20 software. The reported contact angles represented average data from at least five measurements; the standard deviation was also calculated.

**High-Speed Imaging Observation Experiment:** In the experiment, a high-speed machine vision camera with a microscopic lens (Cyclone-IHS-3500, 3500 fps with  $1280 \times 860$  pixels, Optronis GmbH, Germany) was used to record the evolution of droplet wetting at atmospheric pressure. The measurement temperature and relative humidity were within  $25 \pm 1 \text{ }^\circ\text{C}$  and  $50 \pm 5\%$ , respectively. Scanning electron images of the PDMS sample were obtained by using a field emission scanning electron microscope (Zeiss Merlin, Germany).

## Supporting Information

Supporting Information is available from the Wiley Online Library or from the author.

## Acknowledgements

This work was supported by the National Natural Science Foundation of China (Grant No 11972034), the Strategic Priority Research Program of the Chinese Academy of Sciences (Grant No XDB22040301), the Research Program of Beijing (Grant No Z161100002616034), and the Youth Innovation Promotion Association of the Chinese Academy of Science (Grant No 2020018).

## Conflict of Interest

The authors declare no conflict of interest.

## Data Availability Statement

The data that support the findings of this study are available from the corresponding author upon reasonable request.

## Keywords

directional wetting transition, metastable interfaces, microcavity surfaces, power law

Received: February 1, 2021

Revised: April 5, 2021

Published online:

- [1] R. Blossey, *Nat. Mater.* **2003**, *2*, 301.
- [2] D. Wang, Q. Sun, M. J. Hokkanen, C. Zhang, F. Y. Lin, Q. Liu, S. P. Zhu, T. Zhou, Q. Chang, B. He, Q. Zhou, L. Chen, Z. Wang, R. H. A. Ras, X. Deng, *Nature* **2020**, *582*, 55.
- [3] Q. Li, L. Li, K. Shi, B. Yang, X. Wang, Z. Shi, D. Tan, F. Meng, Q. Liu, S. Hu, Y. Lei, S. Liu, L. Xue, *Adv. Sci.* **2020**, *7*, 2001650.
- [4] H. Xie, H.-X. Huang, H.-Y. Mi, *Mater. Lett.* **2018**, *221*, 123.
- [5] H. Dai, Z. Dong, L. Jiang, *Sci. Adv.* **2020**, *6*, eabb5528.
- [6] P. Kant, H. Müller-Groeling, D. Lohse, *Phys. Rev. Lett.* **2020**, *125*, 184501.
- [7] H.-N. Yang, C.-C. Tan, Z.-H. Jia, Z.-T. Zhang, *Appl. Surf. Sci.* **2017**, *394*, 149.
- [8] Y. Sun, X. Sui, Y. Wang, W. Liang, F. Wang, *Langmuir* **2020**, *36*, 14483.
- [9] N. Miljkovic, R. Enright, Y. Nam, K. Lopez, N. Dou, J. Sack, E. N. Wang, *Nano Lett.* **2013**, *13*, 179.
- [10] X. Lin, J. Hong, *Adv. Mater. Interfaces* **2019**, *6*, 1900126.
- [11] H. Chen, T. Ran, Y. Gan, J. Zhou, Y. Zhang, L. Zhang, D. Zhang, L. Jiang, *Nat. Mater.* **2018**, *17*, 935.
- [12] J. Li, X. Zhou, J. Li, L. Che, J. Yao, G. Mchale, M. K. Chaudhury, Z. Wang, *Sci. Adv.* **2017**, *3*, eaao3530.
- [13] Z. Huang, Q. Yang, M. Su, Z. Li, X. Hu, Y. Li, Q. Pan, W. Ren, F. Li, Y. Song, *Adv. Mater.* **2018**, *30*, 1802172.
- [14] C. T. Riche, E. J. Roberts, M. Gupta, R. L. Brutchey, N. Malmstadt, *Nat. Commun.* **2016**, *7*, 10780.
- [15] J. Sun, Y. Li, G. Liu, F. Chu, C. Chen, Y. Zhang, H. Tian, Y. Song, *Langmuir* **2020**, *36*, 9952.
- [16] Z. Nie, E. Kumacheva, *Nat. Mater.* **2008**, *7*, 277.
- [17] M. Yoshino, T. Matsumura, N. Umehara, Y. Akagami, S. Aravindan, T. Ohno, *Wear* **2006**, *260*, 274.
- [18] H. A. Stone, A. D. Stroock, A. Ajdari, *Annu. Rev. Fluid Mech.* **2004**, *36*, 381.
- [19] S. J. Kim, J. Kim, M.-W. Moon, K.-R. Lee, H.-Y. Kim, *Phys. Fluids* **2013**, *25*, 092110.
- [20] Q.-Z. Yuan, X. Huang, Y.-P. Zhao, *Phys. Fluids* **2014**, *26*, 092104.
- [21] Q.-Z. Yuan, Y.-P. Zhao, *J. Fluid Mech.* **2013**, *716*, 171.
- [22] T.-M. Cai, Z.-H. Jia, H.-N. Yang, G. Wang, *Colloid Polym. Sci.* **2016**, *294*, 833.
- [23] H. Kusumaatmaja, R. J. Vrancken, C. W. M. Bastiaansen, J. M. Yeomans, *Langmuir* **2008**, *24*, 7299.
- [24] Y. Wu, F. Wang, S. Ma, M. Selzer, B. Nestler, *Soft Matter* **2020**, *16*, 6115.
- [25] B. Ma, L. Shan, M. B. Dogruoz, D. Agonafer, *Langmuir* **2019**, *35*, 11.
- [26] G. Fang, W. Li, X. Wang, G. Qiao, *Langmuir* **2008**, *24*, 11651.
- [27] L. Courbin, E. Denieul, E. Dressaire, M. Roper, A. Ajdari, H. A. Stone, *Nat. Mater.* **2007**, *6*, 661.
- [28] T. Li, X. Liu, H. Zhao, B. Zhang, L. Wang, *Europhys. Lett.* **2018**, *123*, 36003.
- [29] R. Raj, S. Adera, R. Enright, E. N. Wang, *Nat. Commun.* **2014**, *5*, 4975.
- [30] A. Kumar, R. Raj, *Langmuir* **2017**, *33*, 4854.
- [31] B. Emami, A. A. Hemeda, M. M. Amrei, A. Luzar, M. Gad-el-Hak, H. Vahedi Tafreshi, *Phys. Fluids* **2013**, *25*, 062108.
- [32] P. Lv, Y. Xue, Y. Shi, H. Lin, H. Duan, *Phys. Rev. Lett.* **2014**, *112*, 196101.



- [33] S. Arunachalam, Z. Ahmad, R. Das, H. Mishra, *Adv. Mater. Interfaces* **2020**, *7*, 2001268.
- [34] Y. Xue, S. Chu, P. Lv, H. Duan, *Langmuir* **2012**, *28*, 9440.
- [35] S. U. Cho, D. I. Kim, W. K. Cho, B. S. Shin, M. Y. Jeong, *ACS Appl. Mater. Interfaces* **2016**, *8*, 29770.
- [36] H. Mishra, A. M. Schrader, D. W. Lee, A. Gallo, S. Chen, Y. Kaufman, S. Das, J. N. Israelachvili, *ACS Appl. Mater. Interfaces* **2016**, *8*, 8168.
- [37] T. Y. Liu, C. J. Kim, *Science* **2014**, *346*, 1096.
- [38] S. Arunachalam, R. Das, J. Nauruzbayeva, E. M. Domingues, H. Mishra, *J. Colloid Interface Sci.* **2019**, *534*, 156.
- [39] R. Das, Z. Ahmad, J. Nauruzbayeva, H. Mishra, *Sci. Rep.* **2020**, *10*, 7934.
- [40] E. M. Domingues, S. Arunachalam, H. Mishra, *ACS Appl. Mater. Interfaces* **2017**, *9*, 21532.
- [41] E. M. Domingues, S. Arunachalam, J. Nauruzbayeva, H. Mishra, *Nat. Commun.* **2018**, *9*, 3606.
- [42] P. Pendyala, H. N. Kim, Y. S. Ryu, E. S. Yoon, *ACS Appl. Mater. Interfaces* **2020**, *12*, 39881.
- [43] Y. S. Ryu, D. Yoo, N. J. Wittenberg, L. R. Jordan, S. D. Lee, A. N. Parikh, S. H. Oh, *J. Am. Chem. Soc.* **2015**, *137*, 8692.
- [44] L. K. Malla, N. D. Patil, R. Bhardwaj, A. Neild, *Langmuir* **2017**, *33*, 9620.
- [45] J. B. Lee, S. H. Lee, *Langmuir* **2011**, *27*, 6565.
- [46] P. S. Forsberg, C. Priest, M. Brinkmann, R. Sedev, J. Ralston, *Langmuir* **2010**, *26*, 860.
- [47] Y. H. Mori, T. G. M. van de Ven, S. G. Mason, *Colloids Surf.* **1982**, *4*, 1.
- [48] J. F. Oliver, C. Huh, S. G. Mason, *J. Colloid Interface Sci.* **1977**, *59*, 568.
- [49] J. Fan, J. De Coninck, H. Wu, F. Wang, *Phys. Rev. Lett.* **2020**, *124*, 125502.
- [50] Z. L. Wang, K. Lin, Y. P. Zhao, *J. Colloid Interface Sci.* **2019**, *552*, 563.
- [51] R. W. Style, C. Hyland, R. Boltyanskiy, J. S. Wettlaufer, E. R. Dufresne, *Nat. Commun.* **2013**, *4*, 2728.
- [52] M. Heshmati, M. Piri, *Langmuir* **2014**, *30*, 14151.
- [53] T. C. Ransohoff, C. J. Radke, *J. Colloid Interface Sci.* **1988**, *12*, 392.
- [54] Y. Xiang, Y. Xue, P. Lv, D. Li, H. Duan, *Soft Matter* **2016**, *12*, 4241.
- [55] J. Crank, *The Mathematics of Diffusion*, Oxford University Press, Oxford, UK **1975**.
- [56] P. Atkins, J. de Paula, *Atkins' Physical Chemistry*, 8th ed., Oxford University Press, Oxford, UK **2006**.
- [57] M. Xu, G. Sun, C. J. Kim, *Phys. Rev. Lett.* **2014**, *113*, 136103.
- [58] H. Rahn, C. V. Paganelli, *Respir. Physiol.* **1968**, *5*, 145.
- [59] C. Ding, Y. Fan, *Chin. J. Chem. Eng.* **2011**, *19*, 205.